

Influence of nondimensional heating volume on efficiency of plasma synthetic jet actuators

Zong, Haohua

DOI

[10.2514/1.J056690](https://doi.org/10.2514/1.J056690)

Publication date

2018

Document Version

Accepted author manuscript

Published in

AIAA Journal

Citation (APA)

Zong, H. (2018). Influence of nondimensional heating volume on efficiency of plasma synthetic jet actuators. *AIAA Journal*, 56(5), 2075-2078. <https://doi.org/10.2514/1.J056690>

Important note

To cite this publication, please use the final published version (if applicable). Please check the document version above.

Copyright

Other than for strictly personal use, it is not permitted to download, forward or distribute the text or part of it, without the consent of the author(s) and/or copyright holder(s), unless the work is under an open content license such as Creative Commons.

Takedown policy

Please contact us and provide details if you believe this document breaches copyrights. We will remove access to the work immediately and investigate your claim.

Influence of Nondimensional Heating Volume on Efficiency of Plasma Synthetic Jet Actuators

Haohua Zong*

Delft University of Technology, 2629 HS Delft, The Netherlands

1. Introduction

Plasma flow control has received an overwhelming attention from the active flow control community during the last decade, due to promising application prospects in boundary layer transition control, lift augmentation, drag reduction, noise mitigation and so on [1-2]. Effective flow control relies on the proper selection of actuators. As a representative type of plasma actuators, plasma synthetic jet actuator (PSJA) features the unique combination of high jet velocity (>300 m/s) and high actuation frequency (>5 kHz), thus tailored for high-Reynolds-number supersonic applications [3-4]. Laboratory tests performed by Greene et al. and Narayanaswamy et al. have shown that for shock wave/boundary layer interaction formed by a compression ramp in a Mach 3 flow, the pitched and skewed PSJ is able to reduce the distance between separation line and compression corner by 40% meanwhile decrease the amplitude of low-frequency fluctuation associated with the unsteady separated flow by 30% [5-6].

However, a noticeable weakness of PSJA is the low energy efficiency ($O(0.1\%)$), which has to be improved by the optimal design of actuator geometries [7]. As jet orifice diameter increases, the jet duration time decreases while the peak jet velocity and the electromechanical efficiency remains unchanged [8]. Electrode distance (typical range: $l_a=0.5-3$ mm) and cavity volume (typical range: $V_{ca}=20-2000$ mm³) have also been reported to significantly affect the peak jet velocity and the jet duration time [9]. Nevertheless, their explicit relations with the energy efficiency are still unclear. In the present study, electrical measurements and phase-locked planar Particle Imaging Velocimetry (PIV) measurements are adopted to investigate the effects of electrode distance (l_a) and cavity volume (V_{ca}) on the electromechanical efficiency of PSJA in a large parameter space ($l_a=1-8$ mm; $V_{ca}=50-942$ mm³).

2. Experimental Setup

A. Actuators and Power Supply system

Two actuators with distinct geometrical configurations are tested, as shown in Figure 1. The large-cavity actuator mainly consists of a flat-plate cap (thickness: 3 mm) and a cubic cavity (dimension: $15\times 15\times 15$ mm³), both of which are made of machinable glass ceramic (MACOR) and can be assembled together through a step groove. The inner diameter (D_{ca}) and height (L_{ca}) of the cubic cavity are 10 mm and 12 mm respectively,

* Phd candidate in Faculty of Aerospace Engineering, Delft University of Technology; Email: h.zong-1@tudelft.nl

resulting in a fixed cavity volume (V_{ca}) of 942 mm³. Three holes (diameter: 1 mm) are drilled in the centers of the two side surfaces and the bottom surface. The two opposing holes accommodate two electrodes (anode and cathode), while the bottom hole is connected with a thin capillary (inner diameter: 0.4 mm) which seeds particles inside the cavity during PIV measurements. The spacing between the two electrodes (l_a) can be adjusted between 1-8 mm. A cylindrical orifice (diameter: $D_{ex}=1.5$ mm) is created on the flat-plate cap, acting as the jet exit.

The small-cavity actuator is inherited from Zong et al. [7] thus only a brief description is provided. A ceramic block and two ceramic cylinders are combined together to form an enclosed cavity. The inner diameter of the actuator cavity (D_{ca}) is fixed as 4 mm, whereas the cavity length (also denoted as L_{ca}) can be adjusted between 4 mm and 12 mm by sliding the two ceramic cylinders (V_{ca} : 50-150 mm³). Two tungsten needles (diameter: 1 mm) are inserted through the center holes of the two ceramic cylinders, serving as the anode and the cathode respectively. The spacing between these two electrodes (l_a) can be varied independently from the cavity length. No extra seeding hole is drilled for this actuator, and PIV particles are fed inside the actuator cavity through the radial clearance between tungsten needles and ceramic cylinders (0.1 mm). The jet exit is located in the middle of the actuator cavity, with neck length of 3 mm. The exit orifice diameter of this small-volume actuator (1 mm) differs from that of the large-volume actuator (1.5 mm). Nevertheless, it will not interfere with the parametric studies of cavity volume and electrode distance, as orifice diameter plays a negligible role in the efficiency characteristics of PSJA during the single-shot operation mode [8]. A cylindrical coordinate system is established in the jet exit center as shown in Figure 1, with r -axis and x -axis along the radial and the axial direction respectively.

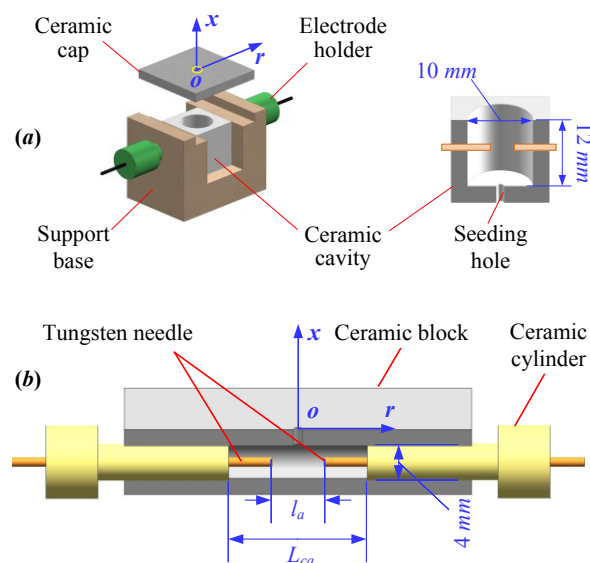


Figure 1 (a) Large-cavity actuator; (b) Small-cavity actuator

A sequential discharge power supply (trigger discharge-capacitive discharge) proposed by Zong & Kotsonis is deployed to implement the energy deposition [10]. For the large-cavity actuator, an energy-storing capacitor with capacitance (C_1) of $1\mu\text{F}$ is connected in the discharge circuit and the capacitor voltage (U_c) is charged to 2 kV before ignition. In contrast, C_1 and U_c are reduced to $0.1\mu\text{F}$ and 0.25kV respectively to feed the small-cavity actuator. Under both circumstance, the arc voltage (U_d) and the discharge current (I_d) at increasing electrode distance are measured by a high-voltage probe (Tektronix, P6015A) and a current monitor (Pearson, Model 325) respectively, and recorded by an oscilloscope (Tektronix, TDS 3054C). At $C_1=1\mu\text{F}$, $U_c=2\text{kV}$ and $l_a=2\text{ mm}$, representative discharge waveforms are shown in Figure 2 (a).

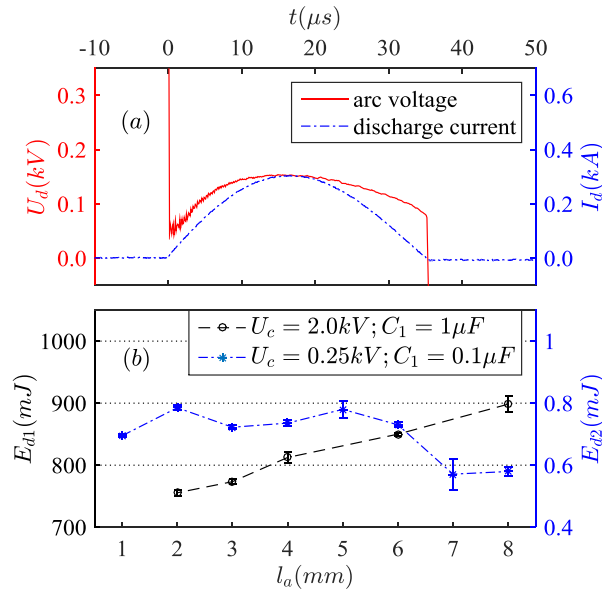


Figure 2 (a) Representative discharge waveforms at $C_1=1\mu\text{F}$, $U_c=2\text{kV}$ and $l_a=2\text{ mm}$. (b) Variation of the discharge energy (E_{d1} and E_{d2}) with electrode distance.

The discharge current exhibits a half-sinusoidal shape with a peak value of 305 A and duration of 35 μs . The arc voltage follows the variation trend of the discharge current, ranging from 50-150 V. The integral of the discharge power ($U_d I_d$) with time defines the discharge energy (E_d), as shown in Equation (1).

$$E_d = \int_0^{T_d} U_d(t) I_d(t) \cdot dt \quad (1)$$

Where T_d denotes the discharge duration. Subscripts are added to distinguish the large-capacitor cases (E_{d1}) from the small ones (E_{d2}). As show in Figure 2 (b), E_{d1} increases monotonically with increasing electrode distance, whereas E_{d2} experiences a small-magnitude fluctuation between 0.7 mJ and 0.8 mJ at $l_a \leq 6\text{ mm}$ and drops to approximately 0.6 mJ afterwards. The dropping trend of E_{d2} is attributed to the increasing residual capacitor voltage (not shown). Specifically, due to the rapid increasing arc resistance ($O(10\ \Omega)$), the peak

discharge current in the small energy cases decreases significantly, which results in less energy deposition in the electrode gap and growing residual energy in the energy-storing capacitor. For the cases of large energy deposition, the drop of discharge current with increasing electrode distance is not prominent due to relatively small arc resistance ($O(1 \Omega)$), and the monotonic increase of energy deposition (E_{dl}) is directly related to the improving discharge efficiency.

B. PIV system

A phase-locked PIV system consisting of a CCD camera (Imperx Bobcat IGV-B1610, sensor resolution: 1628×1236 pixels, pixel pitch: $4.4 \mu\text{m}$), a single head Nd:YAG laser (Quantel EverGreen, peak pulse energy: 200 mJ) and a programmable timing unit (Lavision, PTU9) are deployed to measure the jet induced flow in the xr -plane. The optical configuration, seeding regime and synchronization methods are the same as that in [8, 11], thus will not be described here. The imaged field of view is $12 \times 12 \text{ mm}^2$ for both actuators. An interrogation window size of 24×24 and an overlapping ratio 75% are used in post-processing, resulting in a spatial resolution of 22 vectors/mm. Approximately 20-30 phases are selected to restore the entire evolution of PSJ, starting from the emanation of incipient jets and terminating at the presence of suction flow. For each phase, 200 image pairs are acquired to get statistically converged mean velocity field.

Table 1. Test scheme in PIV measurements

Group No.	Conditions	Tested parameters
1	$C_I=1 \mu\text{F}$; $U_c=2 \text{ kV}$; $D_{ca}=10 \text{ mm}$; $L_{ca}=12 \text{ mm}$	$l_a=2, 3, 4, 6, 8 \text{ mm}$
2	$C_I=0.1 \mu\text{F}$; $U_c=0.25 \text{ kV}$; $D_{ca}=4 \text{ mm}$; $L_{ca}=10 \text{ mm}$	$l_a=1, 3, 5, 7 \text{ mm}$
3	$C_I=0.1 \mu\text{F}$; $U_c=0.25 \text{ kV}$; $D_{ca}=4 \text{ mm}$; $l_a=3 \text{ mm}$	$L_{ca}=6, 8, 10, 12 \text{ mm}$
4	$C_I=0.1 \mu\text{F}$; $U_c=0.25 \text{ kV}$; $D_{ca}=4 \text{ mm}$; $l_a/L_{ca}=0.5$	$L_{ca}=6, 8, 10, 12 \text{ mm}$

14 cases classified into 4 groups are tested in PIV measurements, as listed in Table 1. Groups 1-2 focus on the effect of electrode distance (l_a) at fixed cavity volume. Group 3 and Group 4 concern the influence of cavity volume under conditions of fixed electrode distance ($l_a=3 \text{ mm}$) and fixed ratio of $l_a/L_{ca}=0.5$, respectively.

3. Results and Discussion

Based on the measured phase-averaged velocity fields (denoted as $u(r,z,t)$), the spatially-averaged exit velocity at a given time delay (denoted as $\underline{U}_{ex}(t)$) can be computed by Equation (2).

$$U_{ex}(t) = \frac{\int_0^{D_{ex}/2} u_x(r,t) \pi r dr}{\pi D_{ex}^2 / 4} \quad (2)$$

The exit velocity traces pertaining to Group 1 are shown in Figure 3 (a). Both the peak jet velocity and the jet duration time (T_{jet}) increases with increasing electrode distance, indicating an improvement in jet intensity. Based on these exit velocity traces, the time-varying exit density ($\rho_{ex}(t)$) can be estimated using the model proposed in [8]. The combination of the exit velocity and the exit density enables the computation of jet kinetic energy (E_m). The ratio of jet kinetic energy to discharge energy defines the electro-mechanical efficiency (η_m), as shown in Equation (3) where A_{ex} is the area of jet exit.

$$\begin{cases} E_m = 0.5 \cdot \int_0^{T_{jet}} \rho_{ex}(t) A_{ex} U_{ex}^3(t) dt \\ \eta_m = E_m / E_d \end{cases} \quad (3)$$

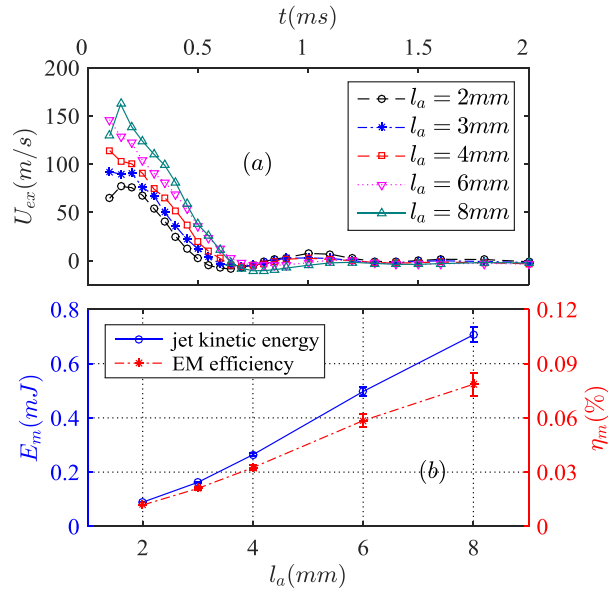


Figure 3 (a) Time evolution of the mean exit velocity pertaining to Group 1. (b) Variation of the electromechanical efficiency (EM efficiency) in Group 1

Figure 3 (b) shows the jet kinetical energy and the electromechanical efficiency for Group 1. Both E_m and η_m increase linearly with the electrode distance, which can be attributed to the expanding heating volume [7]. Specifically, the pulsed arc discharge used to pressurize the cavity gas is confined locally in the electrode gap. As a result of this localized arc heating, multiple shock waves are created, propagating and reflecting in the

actuator cavity. On the one hand, the propagating shock waves pressurize the cavity gas far away from the discharge region. On the other hand, a large portion of the mechanical energy is dissipated since it is a non-isentropic process. When the electrode distance increases, the heating volume expands and the pressure distribution in the actuator cavity becomes more uniform. As a result, the propagation distance of the arc-induced shock waves decreases and the shock wave intensity drops, leading to an increasing electromechanical efficiency.

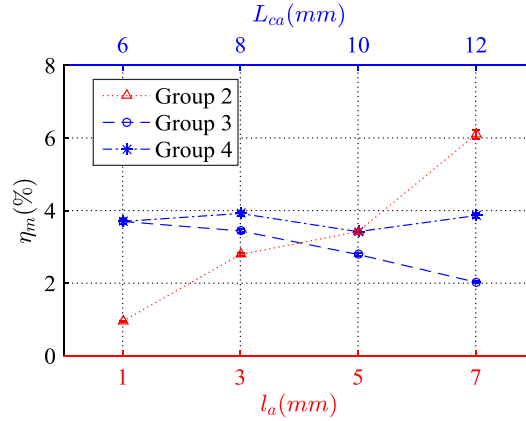


Figure 4 Variation of the electromechanical efficiency in Groups 2-4.

Variation of the electromechanical efficiency in Groups 2-4 are shown in Figure 4. The benefit of increasing electrode distance to η_m is also valid for the small-cavity actuator (Group 2). When the electrode distance remains unchanged and the cavity length increases (Group 3), η_m drops steadily which is attributed again to the increasing propagation distance of arc-induced shock waves. In Group 4, the ratio of electrode distance to cavity length is kept constant and the four tested cases exhibit similar electromechanical efficiency. These variation trends indicate that the ratio of arc heating volume to cavity volume (denoted as ξ , nondimensional heating volume) plays a significant role in the electromechanical efficiency. The relation between geometrical parameters and ξ is as follows,

$$\xi = \frac{l_a d_a^2}{L_{ca} D_{ca}^2} \quad (4)$$

Where, d_a represents the mean arc diameter. For the small and large energy cases, d_a can be estimated as 0.6 mm and 1.0 mm respectively [12].

In Figure 5, η_m is plotted against ξ . As expected, the data from Groups 2-4 collapse together and can be fitted by a line. Hence, the relation between η_m and ξ can be described by power functions. Exponents of these power functions are fitted to be 1.4 and 0.86 for the large-cavity actuator and the small-cavity actuator,

respectively. Comparing the datasets from the two actuators, it is striking to notice that the efficiency values of the small-cavity actuator are approximately 30 times higher than that of the large-cavity actuator at same ξ . This indicates that the effect of cavity volume is considerably nonlinear. A simply combination of geometrical parameters (namely the nondimensional heating ratio) can only account for the losses caused by arc induced shock waves in small range (V_{ca} : 50-150 mm³).

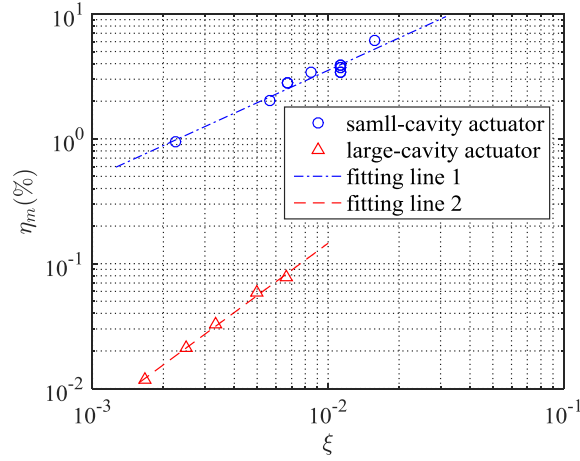


Figure 5 Variation of electromechanical efficiency with nondimensional heating volume

Apart from the localized arc heating considered earlier, the different discharge timescales and discharge energy should also be incorporated to interpret the distinction of η_m between the tested two actuators. Specifically, the discharge duration for large energy cases (35 μ s, see Figure 2 (a)) is approximately ten times longer than that in small energy cases (approximately 3 μ s, not shown) as a result of increasing capacitance. This long-duration discharge makes the energy deposition process deviate severely from the constant-volume heating process, which leads to a low thermal cycle efficiency [7]. Additionally, with increasing discharge energy, both the arc temperature and the arc diameter increase considerably. This accelerates the dissipation of arc heating energy to surrounding environment and results in a decreasing heating efficiency.

4. Conclusions

Influence of geometrical parameters on the electromechanical efficiency of PSJA (η_m) is investigated with electrical measurements and phase-locked planar PIV measurements. Two actuators with changeable electrode distance are tested. The first actuator features a fixed cavity volume (V_{ca}) of 942 mm³, whereas for the second actuator, V_{ca} can be adjusted between 50 mm³ and 150 mm³. As a result, η_m improves significantly with increasing nondimensional heating volume (ξ , ratio of heating volume to cavity volume) for both actuators. At the same value of ξ , the efficiency of the small-cavity actuator ($O(1\%)$) are approximately 30 times higher than that of the large-

cavity actuator ($O(0.01\%)$), which is mainly ascribed to the losses caused by arc induced shock waves. From the perspective of energy efficiency, long electrode distance and small cavities in elongated shapes are recommended in the actuator design due to the considerable difficulty in producing long diffused arcs.

References

- [1]. Corke, T. C., Enloe, C. L., & Wilkinson, S. P. (2010). Dielectric barrier discharge plasma actuators for flow control. *Annual review of fluid mechanics*, 42, 505-529. DOI: 10.1146/annurev-fluid-121108-145550
- [2]. Cattafesta III, L. N., & Sheplak, M. (2011). Actuators for active flow control. *Annual Review of Fluid Mechanics*, 43, 247-272. DOI: 10.1146/annurev-fluid-122109-160634
- [3]. Grossman, K., Bohdan, C., & VanWie, D. (2003). Sparkjet actuators for flow control. In *41st Aerospace Sciences Meeting and Exhibit* (p. 57). DOI: 10.2514/6.2003-57
- [4]. Narayanaswamy, V., Raja, L. L., & Clemens, N. T. (2010). Characterization of a high-frequency pulsed-plasma jet actuator for supersonic flow control. *AIAA journal*, 48(2), 297-305. DOI: 10.2514/1.41352
- [5]. Greene, B. R., Clemens, N. T., Magari, P., & Micka, D. (2015). Control of mean separation in shock boundary layer interaction using pulsed plasma jets. *Shock Waves*, 25(5), 495-505. DOI: 10.1007/s00193-014-0524-5
- [6]. Narayanaswamy, V., Raja, L. L., & Clemens, N. T. (2012). Control of unsteadiness of a shock wave/turbulent boundary layer interaction by using a pulsed-plasma-jet actuator. *Physics of Fluids*, 24(7), 076101. DOI: 10.1063/1.4731292
- [7]. Zong, H., Wu, Y., Song, H., & Jia, M. (2016). Efficiency characteristic of plasma synthetic jet actuator driven by pulsed direct-current discharge. *AIAA Journal*, 3409-3420. DOI: 10.2514/1.J054987
- [8]. Zong, H., & Kotsonis, M. (2016b). Electro-mechanical efficiency of plasma synthetic jet actuator driven by capacitive discharge. *Journal of Physics D: Applied Physics*, 49(45), 455201. DOI: 10.1088/0022-3727/49/45/455201
- [9]. Cybyk, B., Grossman, K., & Van Wie, D. (2003, June). Computational assessment of the sparkjet flow control actuator. In *33rd AIAA Fluid Dynamics Conference and Exhibit* (p. 3711). DOI: 10.2514/6.2003-3711
- [10]. Zong, H., & Kotsonis, M. (2017). Realisation of plasma synthetic jet array with a novel sequential discharge. *Sensors and Actuators A: Physical*, 266: 314-317. DOI: 10.1016/j.sna.2017.09.027
- [11]. Zong, H., & Kotsonis, M. (2016a). Characterisation of plasma synthetic jet actuators in quiescent flow. *Journal of Physics D: Applied Physics*, 49(33), 335202. DOI: 10.1088/0022-3727/49/33/335202
- [12]. Belinger, A., Naudé, N., Cambronne, J. P., & Caruana, D. (2014). Plasma synthetic jet actuator: electrical and optical analysis of the discharge. *Journal of Physics D: Applied Physics*, 47(34), 345202. DOI: 10.1088/0022-3727/47/34/345202